Thermally Driven Diurnally Periodic Wind Signals off the East Coast of China

YU DU

Laboratory for Climate and Ocean-Atmosphere Studies, Department of Atmospheric and Oceanic Sciences, School of Physics, Peking University, Beijing, China, and National Center for Atmospheric Research, Boulder, Colorado

RICHARD ROTUNNO

National Center for Atmospheric Research, Boulder, Colorado

(Manuscript received 17 November 2014, in final form 6 April 2015)

ABSTRACT

The characteristics of thermally driven diurnally periodic wind signals off the east coast of China are studied using hourly model data for the period June 2006–11 simulated with a mesoscale model. Analysis of these model data indicates low-level diurnally periodic wind signals propagate eastward off the southeast coast, whereas diurnal wind variations off the northeast coast are nearly in phase. It is found that a simple 2D linear land–sea-breeze model with friction can capture this main difference in propagation character with respect to latitude. Idealized simulations using a simplified version of the mesoscale model that includes surface heating and terrain are found to explain certain features not captured by the present linear theory such as the absolute time phase and cross-coast location of the maximum amplitude of the diurnally periodic winds.

1. Introduction

Du et al. (2015b) using a mesoscale model run in ‘‘climate mode’’ studied the diurnal variation of the boundary layer winds near and away from the east coast of China. Closer examination of the Du model data (Du et al. 2014) herein also indicates diurnally periodic offshore propagation of the amplitude and phase of the low-level wind field, but with significant variations with latitude. The present study seeks to explain these features from the Du model data using a variation on the linear sea-breeze theory of Rotunno (1983, hereafter R83) and further developed by Jiang (2012b) to explain general features of sea-breeze-associated offshore propagation.

Offshore propagation of meteorological signals relating to surface winds, stratocumulus, temperature, and precipitation driven by the diurnally varying thermal contrast near the coast have been observed in the tropics or subtropics for a number of years (Yang and Slingo 2001; Gille et al. 2005; Muñoz 2008; Wood et al. 2009; Rahn and Garreaud 2010). Using the Cloud Archive User Service (CLAUS) dataset of brightness temperature, Yang and Slingo (2001) found that a strong diurnal signal (convective activity) over land is spread out over the adjacent sea in the tropics probably through gravity waves. The offshore propagation of diurnal wind variation is significant equatorward of 30° latitude (Gille et al. 2005). Mapes et al. (2003) found that a propagation signal (convection) in the Panama Bight region off the northwestern coast of South American is due to thermally forced gravity waves produced by elevated terrain. Garreaud and Muñoz (2004) in their regional numerical simulations found that a band of upward motion propagates from the southern coast of Peru into the subtropical southeast Pacific during the late afternoon and nighttime.

The propagation of diurnal variations of precipitation and its related flow have been studied over land in China at midlatitudes through observations and modeling studies (e.g., Wang et al. 2004, 2005; Yu et al. 2007; He and Zhang 2010; Bao et al. 2011; Sun and Zhang 2012; Du et al. 2014). In these studies, the prevailing steering flow plays a significant role in the propagation of the diurnal variations. Similar phenomena were also found over the U.S. Great Plains east of the Rocky Mountains (e.g., Carbone et al.

Corresponding author address: Dr. Richard Rotunno, National Center for Atmospheric Research, P.O. Box 3000, Boulder, CO 80307.
E-mail: rotunno@ucar.edu

DOI: 10.1175/JAS-D-14-0339.1

2002; Trier et al. 2006). However, few studies document the propagation of diurnally periodic wind signals off the east coast of China, which spans from the subtropics to midlatitudes. Du et al. (2015b) using a long-term daily simulation dataset (Du et al. 2014; Du model data) analyzed diurnally varying boundary layer winds in eastern China using a simple 1D model proposed by Du and Rotunno (2014). From their Fig. 1 we noticed that the time phase of the diurnal winds off the southeastern coast of China varies with offshore distance (for the same latitude) and seems to be a propagating signal; however, such features are not evidenced off the northeastern coast. This interesting contrast in propagation signals motivates the present study of the thermally driven diurnally periodic wind signals off the east coast of China with a model that is more complicated than the 1D model used in our previous study.

Jiang (2012a) used a linear theory of the land and sea breeze to examine the characteristics and dynamics of offshore diurnal waves induced by land–sea thermal contrast. This type of linear theory has been extensively used to study the atmospheric response to land–sea differential heating (R83; Qian et al. 2009; Drobinski et al. 2011; Jiang 2012b). R83 found that in theory the land–sea breeze should be in the form of internal inertia–gravity waves for latitudes less than 30°, whereas the land–sea breeze should be in the form of a trapped circulation confined to a limited distance from the coastline for latitudes greater than 30°. He also found that both cases became indistinguishable from one another given sufficient friction. Qian et al. (2009) extended the R83 theory to consider an across-coast background wind (but with zero Coriolis force). Drobinski et al. (2011) extended the R83 theory to include an along-coast thermal wind (for latitudes greater than 30°). Jiang (2012b) introduced a three-dimensional linear model to examine the effects of complex coastline shape, Earth's rotation, and background wind. In all of these studies, diurnal heating is represented by a prescribed function, which considerably simplifies the mathematical solutions and interpretations.

In the present study, we use a variation on the aforementioned linear theory in an attempt to explain the main features of thermally driven diurnally periodic wind signals off the east coast of China as seen in the Du model data. Although the linear theory describes many of the features of the Du model data, we found, using a simplified mesoscale model, the inclusion of surface heating, vertical diffusion, and terrain, which are not included in the present linear theory, are needed for a better description of the data.

In section 2, features of diurnal wind signals off the east coast of China are described using the Du model data. An explanation in terms of linear land–sea-breeze theory is discussed in section 3. In section 4, an idealized 2D version of the WRF Model including surface heating and terrain is used as a supplement to the present linear theory that provides a more precise explanation of the Du model data. The results are summarized in section 5.

2. Diurnally periodic wind signals from Du model data

a. *Review of the Du model data*

Du et al. (2014) used the nonhydrostatic Advanced Research version of the Weather Research and Forecasting Model (ARW; Skamarock and Klemp 2008) to generate long-term hourly outputs from daily simulations over China during the early summer (May, June, and July, from 2006 to 2011) with a horizontal grid spacing of 9 km and with 40 vertical levels. The detailed model configuration and integration procedures are given in Du et al. (2014). After evaluation against observations (soundings and wind profiler radars[1]), the dataset was used to study the spatial distribution of low-level jets (LLJs) in China (Du et al. 2014) and diurnal boundary layer winds in eastern China (Du et al. 2015a,b). This dataset captures the propagation of diurnal precipitation east of the Tibetan Plateau (section 5b in Du et al. 2014) that has been observed in several recent studies (e.g., Bao et al. 2011; Xu and Zipser 2011).

b. *Features of the wind signals*

Using the Du model data, we focus on the characteristics of thermally driven diurnally periodic wind signals off the east coast of China, such as time phase, amplitude, and propagation.

Figure 1 shows the diurnal variations of perturbation (with respect to the daily mean value) vertical velocity and perturbation horizontal wind vectors at 950 hPa off the east coast of China. Upward velocity occurs at and near the coast in the evening [1800–2100 local solar time (LST)] and propagates eastward while decaying in the early morning; this propagation signal is more evident off the southeastern coast than off the northeastern coast. The veering of the perturbation wind vectors also corresponds to the features observed in the vertical motion. Off the northeastern coast (near the northern green box in Fig. 1), the perturbation

---

[1] Please see section 2 in Du et al. (2014) and section 3 in Du et al. (2015a) for details of biases and errors.

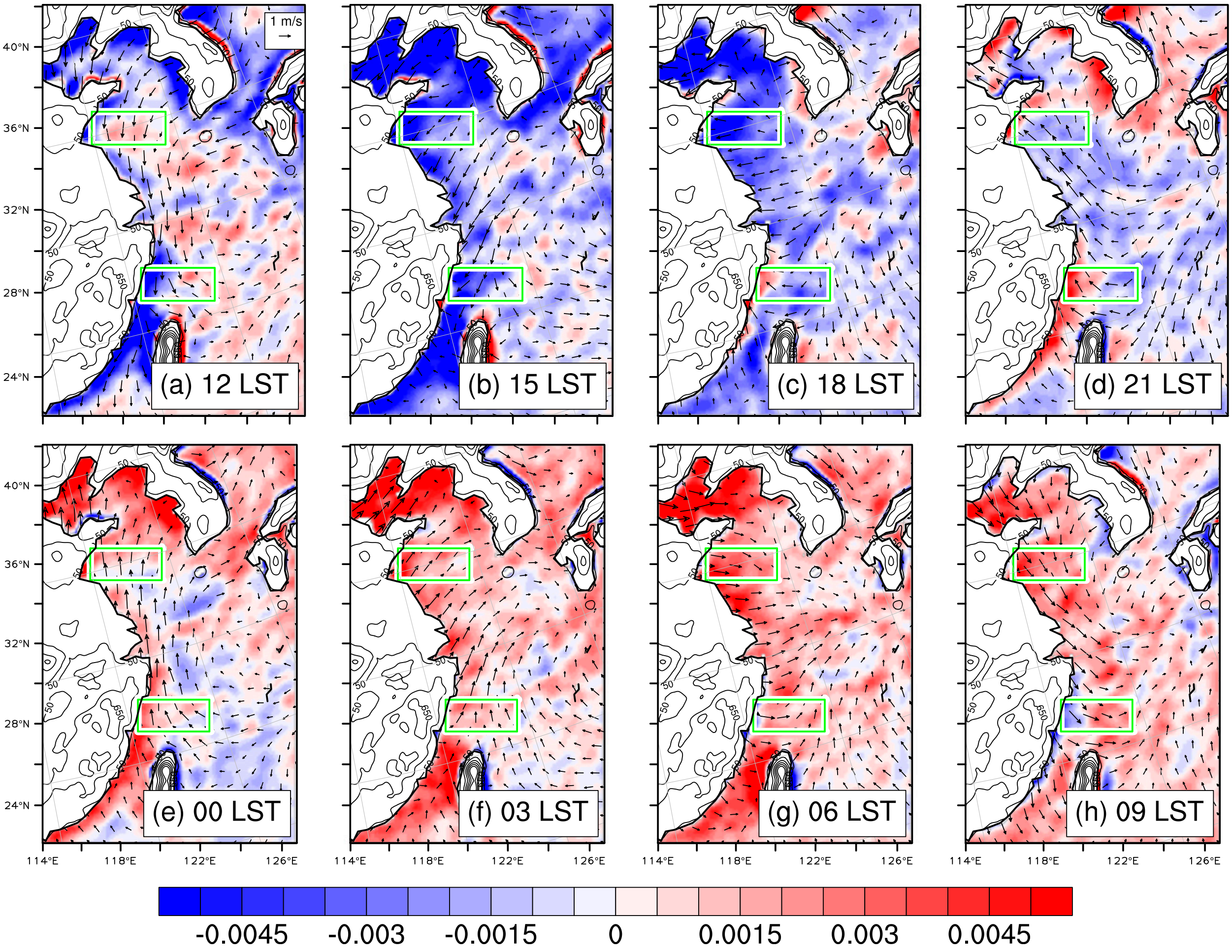

FIG. 1. Diurnal variation of perturbation horizontal wind vectors [reference vector at top right of (a) $=1\,\mathrm{m\,s^{-1}}$] and vertical velocity (color shaded; $\mathrm{m\,s^{-1}}$) at 950 hPa at (a) 1200, (b) 1500, (c) 1800, (d) 2100, (e) 0000, (f) 0300, (g) 0600, and (h) 0900 LST averaged over June 2006–11; selected contours show the terrain height (m) and the two green boxes are used for the analysis in Fig. 2.

diurnal wind vectors all veer with nearly the same time phase, whereas off the southeastern coast (near the southern green box in Fig. 1) the time phase of the perturbation wind vectors varies with offshore distance (for the same latitude).

To see these features more clearly, the longitude (x)–time Hovmöller diagrams of the perturbation vertical motion and wind vectors latitude (y) averaged over the northern and southern boxes of Fig. 1 are shown in Figs. 2a,b. As shown in Fig. 2a, upward vertical motion at 950 hPa in the northern box reaches a maximum in the early morning (0400–0600 LST) at nearly all longitudes (however, at and near the coast the maximum occurs approximately 1–2 h earlier). Correspondingly, the perturbation horizontal winds are almost westerly (easterly) in the early morning (afternoon) without longitudinal variation in direction and become weaker with distance away from the coast. For the southern box, Fig. 2b shows that the diurnal peak of upward vertical motion starts around 2100 LST at and near the coast and then propagates eastward (while decaying) to 400 km away from the coast around 0900 LST. A rough estimate of the propagation speed gives $\sim 9\,\mathrm{m\,s^{-1}}$. The perturbation horizontal winds correspondingly indicate a propagating signal.

Comparing Figs. 2a and 2b, the diurnally periodic wind signals off the east coast of China display different characteristics for the northeastern and the southeastern coasts. The signal of the diurnal winds off the southeastern coast exhibits phase propagation while that off the northeastern coast appears to be phase locked. These features suggest an association with the different land–sea-breeze responses to diurnal heating at higher latitudes (>30°) and lower latitudes (<30°) found by R83 in his linear land–sea-breeze theory. Therefore, in the next section, we attempt to use a variation on that linear theory to explain these features off the east coast of China.

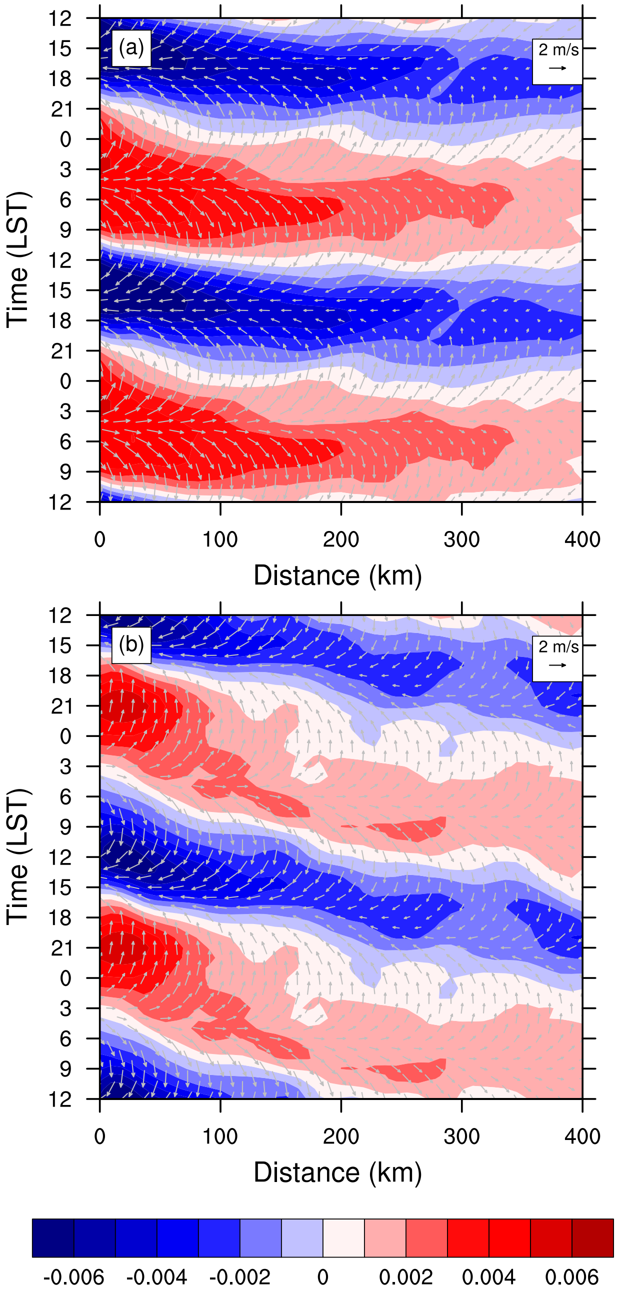

FIG. 2. Longitude distance–time Hovmöller diagrams of perturbation horizontal wind vectors and vertical velocity at 950 hPa (color shaded; $\mathrm{m\,s^{-1}}$) averaged over the (a) northern and (b) southern boxes in Fig. 1 from the Du model data.

3. Possible explanation in terms of the linear land–sea-breeze theory

a. Linear equations and analytical solutions

The 2D linear equations of motion with the shallow, anelastic approximation can be written as (R83)

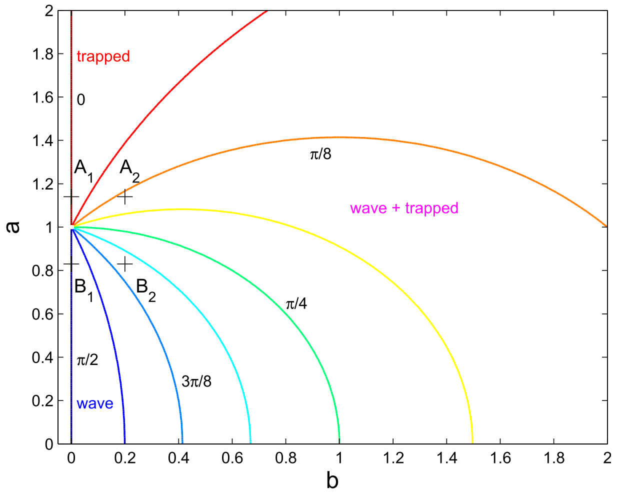

FIG. 3. The phase function χ (different color curves) as a function of a (latitude) and b (friction coefficient). The four crosses show locations of the four points A_1 (35°N, $b = 0$), A_2 (35°N, $b = 0.2$), B_1 (25°N, $b = 0$), and B_2 (25°N, $b = 0.2$).

$$\frac{\partial u}{\partial t} - fv = -\frac{\partial \phi}{\partial x} - \alpha u, \tag{1}$$

$$\frac{\partial v}{\partial t} + fu = -\alpha v, \tag{2}$$

$$\frac{\partial w}{\partial t} - b = -\frac{\partial \phi}{\partial z} - \alpha w, \tag{3}$$

$$\frac{\partial b}{\partial t} + N^2 w = Q - \alpha b, \quad \text{and} \tag{4}$$

$$\frac{\partial u}{\partial x} + \frac{\partial w}{\partial z} = 0, \tag{5}$$

where (u, v, w) are the wind components in the (x, y, z) directions, respectively, ϕ is the geopotential, N is buoyancy frequency, f is the Coriolis parameter, and b is the buoyancy. Here the coastline is at $x = 0$ with land to the left ($x < 0$) and sea to the right facing north. The motion is independent of y. Following Haurwitz (1947) and Schmidt (1947) in their classic studies of the sea breeze, the frictional force (per unit mass) has been simplified to $(\alpha u, \alpha v, \alpha w)$ where α is the frictional coefficient. The heating function is specified as $Q = Q_0[(\pi/2) - \tan^{-1}(x/x_0)]e^{-z/z_0}e^{-i\omega t}$, where the horizontal scale of the land–sea contrast in heating is denoted by x_0 and the vertical scale of the heating is denoted by z_0. The $\omega = 2\pi\ \mathrm{day^{-1}}$, $Q_0\ (\mathrm{m\,s^{-3}})$ is the maximum heating rate (maximum buoyancy producing rate), and $t = 0$ corresponds to noon (R83). The mean flow has been neglected on the grounds that it is very weak (not shown) in the Du model data at low levels in our analysis domains (Fig. 1, green boxes).

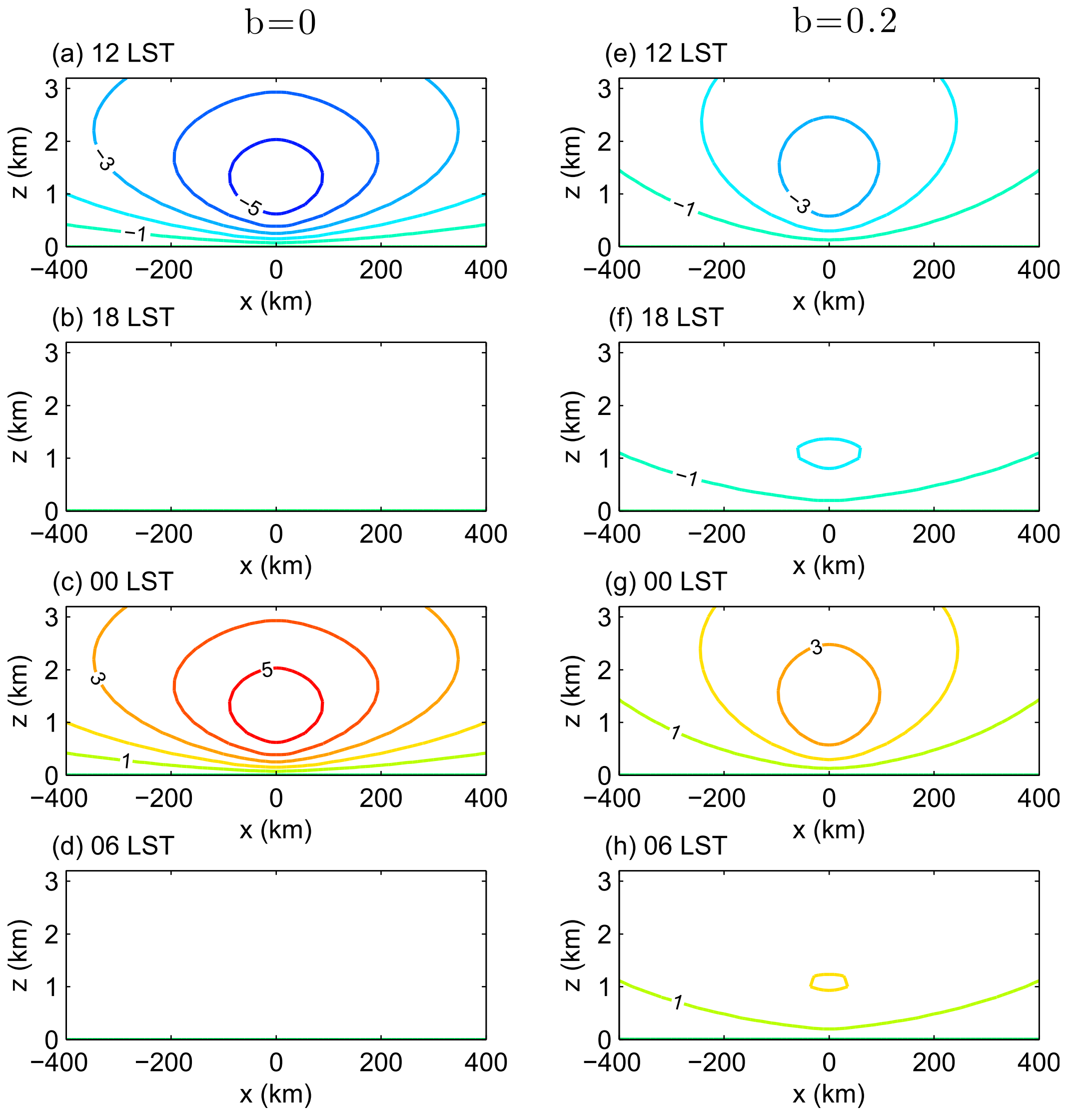

FIG. 4. The x–z structure of the streamfunction over a diurnal cycle at 35°N for (a)–(d) $b = 0$ and (e)–(h) $b = 0.2$ at (a),(e) 1200, (b),(f) 1800, (c),(g) 0000, and (d),(h) 0600. Warm (cold) color means positive (negative) streamfunction.

Equations (1)–(5) can be combined into a single equation for the streamfunction ψ ($u = \partial\psi/\partial z$ and $w = -\partial\psi/\partial x$):

$$\left(\frac{\partial^2}{\partial t^2}+2\alpha\frac{\partial}{\partial t}+\alpha^2+N^2\right)\frac{\partial^2\psi}{\partial x^2}+\left(\frac{\partial^2}{\partial t^2}+2\alpha\frac{\partial}{\partial t}+\alpha^2+f^2\right)\frac{\partial^2\psi}{\partial z^2}$$
$$=-\frac{\partial Q}{\partial x}=Q_0\left(\frac{x_0}{x_0^2+x^2}\right)e^{-z/z_0}e^{-i\omega t}. \qquad (6)$$

It is assumed that $\psi = \mathrm{Re}[\Psi(x, z)e^{-i\omega t}]$ and (6) becomes

$$(-\omega^2-2\alpha\omega i+\alpha^2+N^2)\frac{\partial^2\Psi}{\partial x^2}$$
$$+(-\omega^2-2\alpha\omega i+\alpha^2+f^2)\frac{\partial^2\Psi}{\partial z^2}=Q_0\left(\frac{x_0}{x_0^2+x^2}\right)e^{-z/z_0}. \qquad (7)$$

Taking the Fourier transform of (7) in the x direction—that is, $\hat{\psi}=\int_{-\infty}^{\infty}\Psi e^{-Kx}\,dx$, and letting $\sigma=\omega+i\alpha$—(7) becomes

$$-(N^2-\sigma^2)K^2\hat{\psi}+(f^2-\sigma^2)\frac{\partial^2\hat{\psi}}{\partial z^2}=Q_0\sqrt{\frac{\pi}{2}}e^{-x_0|K|}e^{-z/z_0}. \qquad (8)$$

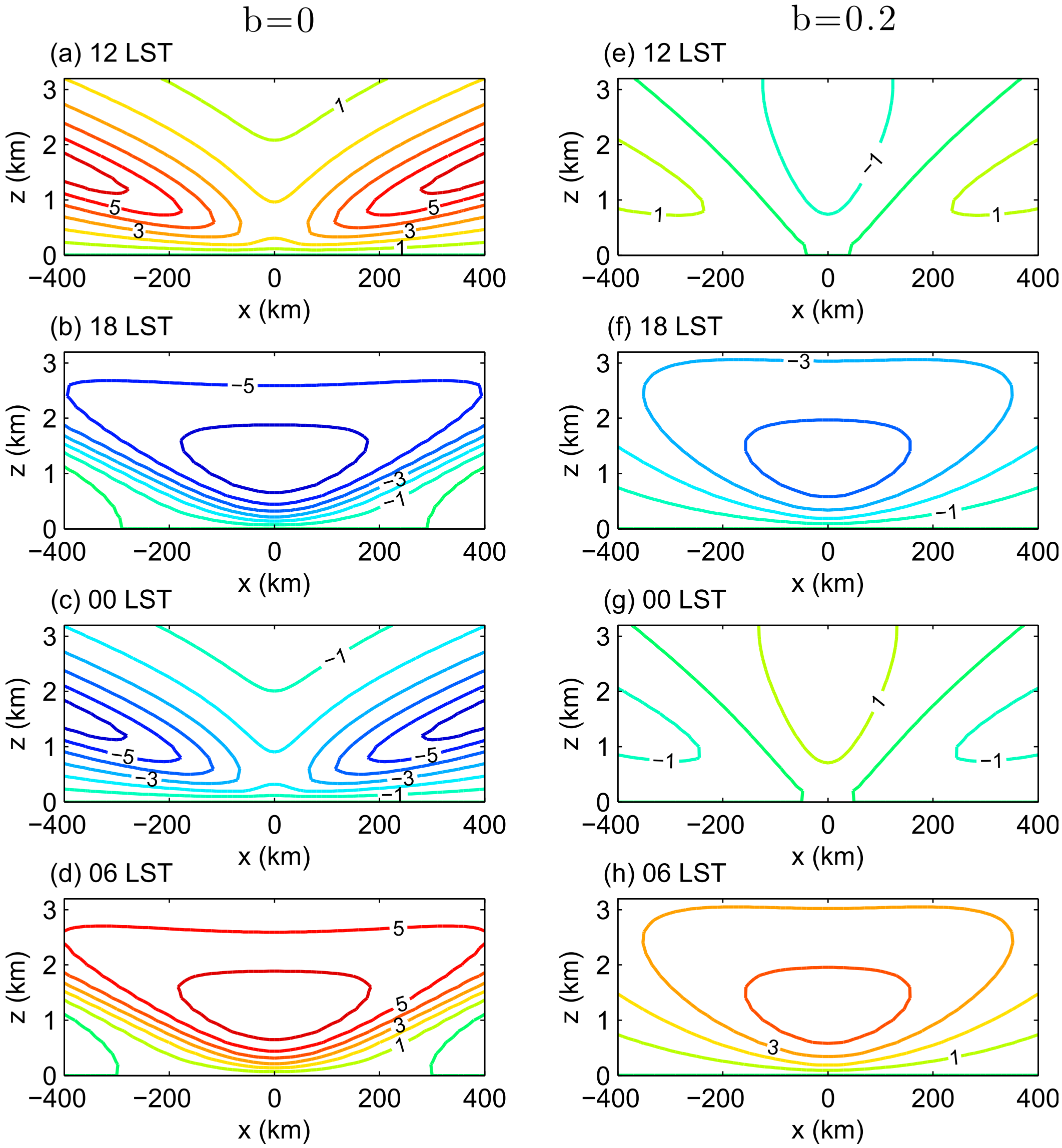

FIG. 5. As in Fig. 4, but for 25°N.

With boundary conditions $\hat{\psi} = 0$ when $z = 0$ and ∞ the solution of (8) is

$$\hat{\psi} = \sqrt{\frac{\pi}{2}}\,\frac{Q_0}{\dfrac{f^2-\sigma^2}{z_0^2} - (N^2-\sigma^2)K^2} \times e^{-x_0|K|}\left[e^{-z/z_0} - e^{-\sqrt{(N^2-\sigma^2)/(f^2-\sigma^2)}\,\mathrm{sgn}(K)Kz}\right]. \tag{9}$$

Applying the inverse Fourier transform, we obtain

$$\psi = \mathrm{Re}\left[\frac{1}{2\pi}\int_{-\infty}^{\infty} \hat{\psi} e^{i(Kx-\omega t)}\, dK\right], \tag{10}$$

$$u = \frac{\partial \psi}{\partial z} = \mathrm{Re}\left(\frac{1}{2\pi}\int_{-\infty}^{\infty} \frac{\partial \hat{\psi}}{\partial z} e^{i(Kx-\omega t)}\, dK\right), \tag{11}$$

$$w = -\frac{\partial \psi}{\partial x} = \mathrm{Re}\left[\frac{i}{2\pi}\int_{-\infty}^{\infty} \hat{\psi} K e^{i(Kx-\omega t)}\, dK\right], \quad \text{and} \tag{12}$$

$$v = \mathrm{Re}\left[\frac{f}{i\omega - \alpha}\,\frac{1}{2\pi}\int_{-\infty}^{\infty} \frac{\partial \hat{\psi}}{\partial z} e^{i(Kx-\omega t)}\, dK\right], \tag{13}$$

which is the solution in physical space. In this study, the integrations indicated above are calculated by numerical method using Matlab.

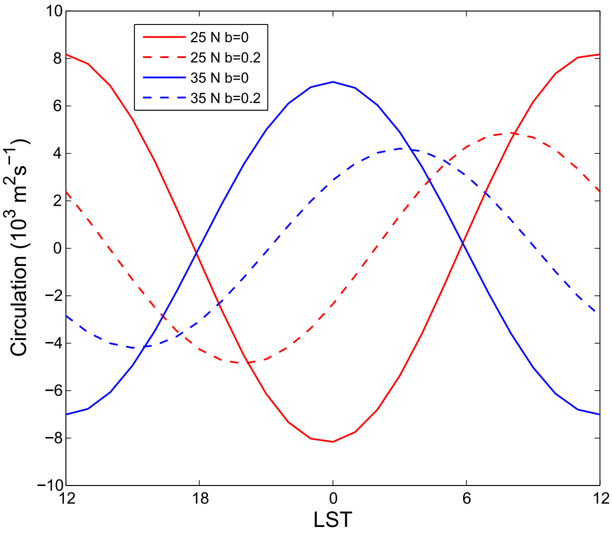

FIG. 6. The diurnal cycle of circulation for $b = 0$ and $b = 0.2$ at 35° and 25°N. Note that the circulation is calculated by averaging u at $z = 0$ along the x direction.

Note that for the homogeneous solution

$$\hat{\psi} \sim e^{-\sqrt{(N^2-\sigma^2)/(f^2-\sigma^2)}\,\mathrm{sgn}(K)Kz},$$

the real and imaginary parts of $\sqrt{(N^2-\sigma^2)/(f^2-\sigma^2)}$ represent, respectively, the damping and the propagation of the wave. Because $N \approx 0.01\,\mathrm{s}^{-1}$, $\omega \approx 0.73 \times 10^{-4}\,\mathrm{s}^{-1}$, and $N^2 \gg \omega^2$, $N^2 \gg \alpha^2$, $\sqrt{(N^2-\sigma^2)/(f^2-\sigma^2)}$ can be written as

$$\begin{aligned}\gamma &= \frac{N}{(f^2-\omega^2+\alpha^2-2\omega\alpha i)^{1/2}}\\ &= -\frac{N}{[(f^2-\omega^2+\alpha^2)^2+4\omega^2\alpha^2]^{1/4}}(\cos\chi - i\sin\chi),\end{aligned}$$

where

$$\begin{aligned}\chi &= \frac{1}{2}\left(\frac{\pi}{2} - \tan^{-1}\frac{f^2-\omega^2+\alpha^2}{2\omega\alpha}\right)\\ &= \frac{1}{2}\left(\frac{\pi}{2} - \tan^{-1}\frac{a^2-1+b^2}{2b}\right)\end{aligned}$$

and the parameters $a = f/\omega$ and $b = \alpha/\omega$ are nondimensional representations of f and α (Du and Rotunno 2014; Du et al. (2015b)). Figure 3 shows χ as function of a (latitude) and b (friction coefficient); the imaginary part of γ indicates wave propagation whereas the real part of γ represents wave damping. When $b = 0$ (no friction), a wave response is found at low latitudes (0°–30°) ($\cos\chi = 0$, $\sin\chi = 1$), whereas a trapped response is found at high latitudes (30°–90°) ($\cos\chi = 1$, $\sin\chi = 0$). The transition between the two regimes is abrupt at latitude 30° ($a = 1$). With b nonzero, all solutions eventually decay far from the source region; however, solutions corresponding to χ near $\pi/2$ are more wavelike while those with χ near zero are closer to being trapped. Figure 3 shows that even for relatively small amount of friction, transition between wavelike and closer-to-trapped solutions at latitude 30° is far more gradual than it is in the frictionless case. Figure 3 is similar to Fig. 8 of Du et al. (2015b), which describes the time phase of the diurnal cycle as a function of latitude and friction. Here we note that this same phase function gives information on wavelike versus closer-to-trapped solutions as a function of latitude and friction.

Based on the latitudes of the two boxes shown in Fig. 1 and the discussion of frictional effects in Du et al. (2015b, p. 722), four points A$_1$ (35°N, $b = 0$), A$_2$ (35°N, $b = 0.2$), B$_1$ (25°N, $b = 0$), and B$_2$ (25°N, $b = 0.2$) in Fig. 3 are chosen for further study of their solution features in next subsection.

b. *Features of land–sea-breeze circulations with friction*

First we compare our solution without friction against the results from R83. We set $\alpha = 0$, $f = 8.342 \times 10^{-5}\,\mathrm{s}^{-1}$ at 35° or $6.146 \times 10^{-5}\,\mathrm{s}^{-1}$ at 25°, $Q_0 = 1.2 \times 10^{-5}\,\mathrm{m\,s}^{-3}$, $z_0 = 1\,\mathrm{km}$, $N = 0.01\,\mathrm{s}^{-1}$, and $x_0 = 50\,\mathrm{km}$ in solution (10) and obtain the diurnal variations of streamfunction in the x–z plane at 35°N (Figs. 4a–d) and 25°N (Figs. 5a–d). In the hydrostatic approximation, the circulation $C(t)$ is given by

$$\begin{aligned}C(t) &= \int_{-\infty}^{\infty}[u(x, z=0, t) - u(x, z=\infty, t)]\,dx\\ &\approx \int_{-\infty}^{\infty} u(x, z=0, t)\,dx\end{aligned}$$

since the contribution from $z = \infty$ is negligible. Figure 6 shows $C(t)$ for the four cases considered here. At 35°N, the streamfunction is confined to near the coast (Figs. 4a–d), and the maximum (minimum, negative) circulation occurs at 0000 LST (1200 LST) (Fig. 6). Note that the oscillation in the cross-coast velocity u has the same phase for any location. Although the heating function is identical to that at 35°N, the structure of the response at 25°N is radically different. The streamfunction is in the form of internal inertia–gravity waves that extend to "infinity" along ray paths extending upward and outward from the coast (Figs. 5a–d). In this case, the oscillation in u does not have the same phase at all points in space. Figure 6 shows that the circulation peaks at 1200 LST, which is a 12-h difference with respect to that of the time phase

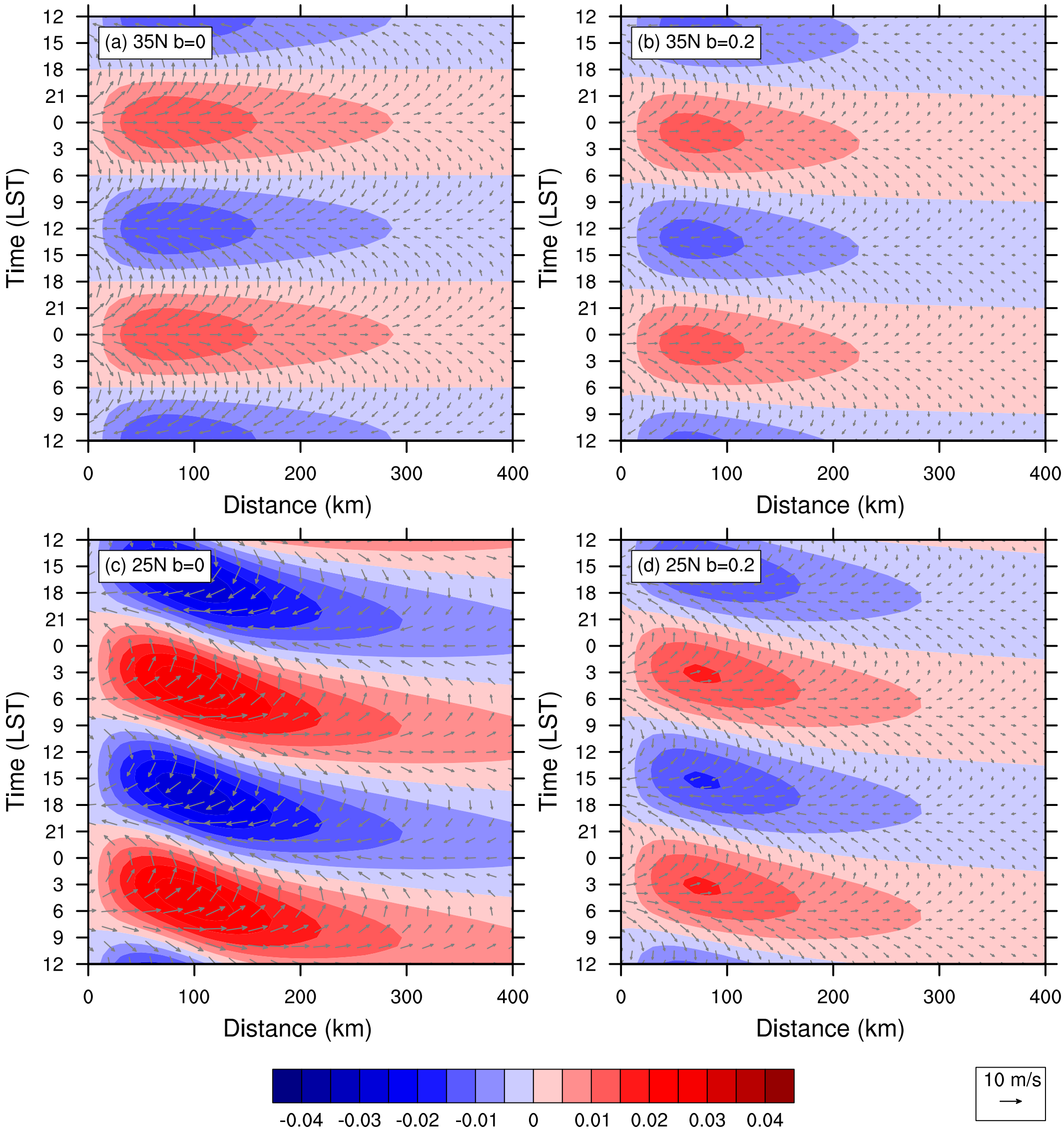

FIG. 7. Longitude distance–time Hovmöller diagrams of perturbation horizontal wind vectors and vertical velocity at 400 m (color shaded; m s^{-1}) from the present linear solutions at (a),(b) 35° and (c),(d) 25°N for (a),(c) $b = 0$ and (b),(d) $b = 0.2$. Distance = 0 is the coast.

of the circulation at 35°N (Fig. 6). These circulations without friction for high latitude and low latitude are consistent with results from R83 (his Fig. 6) and with Fig. 3 at $b = 0$. Jiang (2012a) also documented that wave propagation is less significant at high latitudes than low latitudes in his linear model considering a boundary layer (his Fig. 4).

Figures 4e–h and 5e–h show the diurnal cycles of streamfunction with friction ($b = 0.2$) at 35° and 25°N. The x–z structure and time phase of the streamfunction are both different as compared to their no-friction counterparts. With friction, the strength of the circulation at 35°N is weaker (Figs. 4e–h), and the time phase of circulation lags by 3 h that without friction (Fig. 6). The circulation at 25°N with friction now tends to be more confined to near the coast (Figs. 5e–h) and the time phase of the circulation leads by 4 h that without friction (Fig. 6). Hence the effect of friction is to produce more similarity in the structure and time phase of the solutions northward and southward of 30°N.

The x–t Hovmöller diagrams of the vertical motion and wind vectors at 400-m height are shown in Fig. 7. At 35°N, without friction, the upward vertical motion at 400-m peaks at 0000 LST independent of offshore distance, and the maximum amplitude in the diurnal cycle of vertical motion occurs around 100 km away

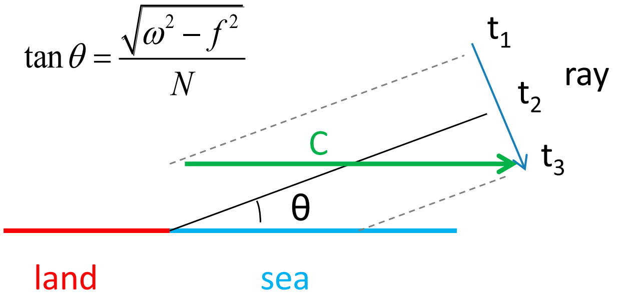

FIG. 8. A schematic diagram showing the movement from t_1 to t_3 of phased lines in the direction perpendicular to the ray path.

from the coast ($x = 100$ km) (Fig. 7a). Correspondingly the perturbation horizontal winds are westerly (easterly) at 0000 LST (1200 LST); more generally, the horizontal winds exhibit no directional variation with x (Fig. 7a). The offshore decay scale is several hundred kilometers, which is consistent with the estimate from (19) of R83,

$$\lambda_H = \frac{Nz_0}{\sqrt{f^2 - \omega^2}} = \frac{10^{-2}\,\mathrm{s}^{-1} \times 1\,\mathrm{km}}{0.4 \times 10^{-4}} \simeq 250\,\mathrm{km},$$

where z_0 corresponds to typical boundary layer depths, which are ~1 km. Those features are also similar to those in obtained in the northern box from Du model data (cf. Fig. 2a). However, the absolute time phases are different and the maximum amplitude in Fig. 7a is not at coast as it is in Fig. 2a. With $b = 0.2$, Fig. 7b indicates that the upward vertical motion exhibits slight phase propagation at 35°N and peaks 1 h later than the no-friction solution at around 100 km (cf. Figs. 7a,b), which is closer to the time phase from the Du model data but still too early (cf. Fig. 7b and Fig. 2a). We note that the magnitude of the solution response is determined in the linear model through the specification of the heating function; hence we focus on the distribution of the velocity in the Hovmöller diagrams but not the magnitude.

At 25°N, Fig. 7c shows that the diurnal peak of upward vertical motion starts at 0000 LST at $x = 0$ and propagates eastward to $x = 400$ km at 1100 LST. A rough estimate of the propagation speed of gives ~10 m s^{-1}, which is close to the estimate from the Du model data (Fig. 2b). A more complete understanding of the wave signal as shown in Fig. 7c can be obtained with following calculation. Following the discussion on p. 2006 of R83, the slope of the ray path is given by the ratio of the group velocity components, which for hydrostatic internal inertia–gravity waves is

$$k/m = (\omega^2 - f^2)^{1/2}/N, \tag{14}$$

where $\omega = [f^2 + (N^2k^2/m^2)]^{1/2}$ is the frequency, k the dominant horizontal, and m the dominant vertical wavenumbers in the wave packet (R83, p. 2006). Of interest for this study is the motion of lines of constant phase that move in the direction perpendicular to the ray path (see blue arrow in Fig. 8). At constant height the horizontal phase speed (green arrow in Fig. 8) is

TABLE 1. WRF Model and physics settings used for the experiments.

	Value							
WRF settings	EXP 1	EXP 2	EXP 3	EXP 4	EXP 5	EXP 6	EXP 7	EXP 8
Heat flux over land (W m^{-2})	20 cosωt, where ω is diurnal frequency, starting time is 1300 LST				100 cosωt, where ω is diurnal frequency, starting time is 1300 LST			
Heat flux over ocean (W m^{-2})	0							
Coriolis parameter (10^{-4} s^{-1})	0.8342	0.6146	0.834	0.6146	0.834	0.6146	0.834	0.615
Vertical diffusion for momentum (m^2 s^{-1})	1		6		60		60 for land 6 for sea	
Horizontal diffusion for momentum and heat (m^2 s^{-1})	0							
Vertical diffusion for heat (m^2 s^{-1})	6				60		60 for land 6 for sea	
Drag coefficient	0							
Moisture flux [g m (kg s)$^{-1}$]	0							
Horizontal resolution (km)	5							
Vertical levels	40							
Long-wave physics	None							
Short-wave physics	None							
Surface scheme	Thermal diffusion scheme							
Surface layer scheme	None							
Cumulus scheme	None							
Microphysics scheme	None							
Initial wind (m s^{-1})	0							
Initial vertical gradient of potential temperature (K km^{-1})	5							

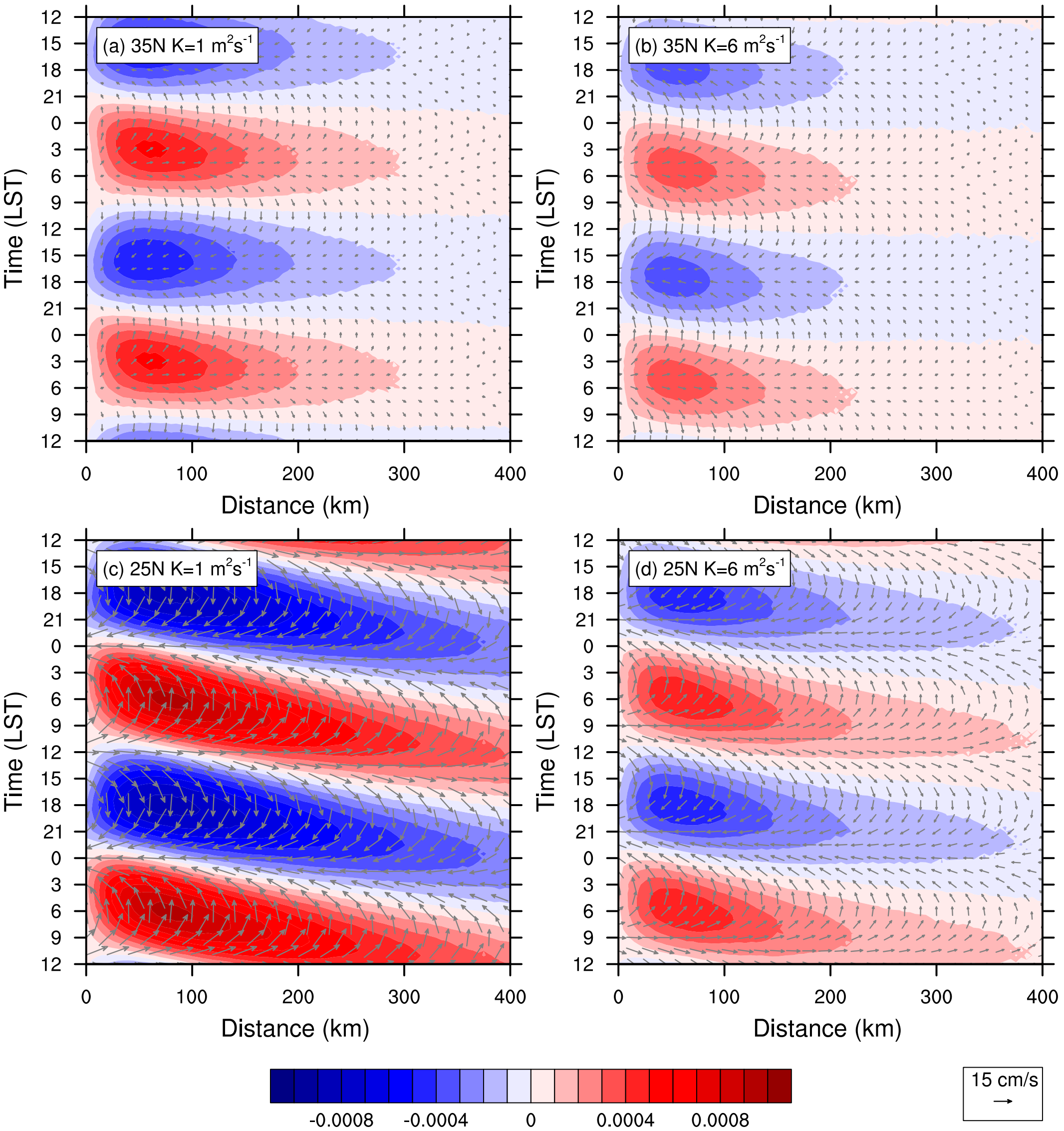

FIG. 9. Longitude distance–time Hovmöller diagrams of perturbation horizontal wind vectors and vertical velocity at 950 hPa (color shaded; m s^{-1}) at (a),(b) 35° and (c),(d) 25°N for vertical diffusion coefficient for momentum equal to (a),(c) 1 and (b),(d) 6 m^2 s^{-1} from the idealized WRF simulations without terrain. The amplitude of diurnal heat fluxes is 20 W m^{-2} and the vertical diffusion coefficient for heat is 6 m^2 s^{-1}.

$$c = \frac{\omega}{k} = \frac{\omega}{m}\frac{N}{\sqrt{\omega^2 - f^2}} = \frac{N\lambda_z}{2\pi\sqrt{1-a^2}}, \qquad (15)$$

where (14) has been used for k, $a = f/\omega = 0.845$ is nondimensional latitude (25°N), and the vertical scale $\lambda_z \propto z_0$. Given that $c \approx 10\,\mathrm{m\,s^{-1}}$ from Fig. 7c, we can that estimate $\lambda_z \simeq 3\,\mathrm{km}$, which is roughly consistent with the structure shown in Figs. 4a–d.

With friction, Fig. 7d indicates that the propagation speed is somewhat faster (i.e., closer to phase locked). The linear-theory propagation signal with or without friction as seen in the vertical motion and wind vectors is similar to that in that analyzed from the Du model data (cf. Figs. 7c,d and Fig. 2b). But, as with the northern case, differences between the theory and the Du model data still exist regarding the absolute time phase and the location of the maximum amplitude.

In summary, as expected in the linear theory, the vertical motion at 25°N exhibits a significant offshore-propagation signal (Figs. 7c,d), whereas the time phase of vertical motion at 35°N is generally independent of the offshore coordinate (Fig. 7a,b). These features successfully capture the main features analyzed from the Du model data. The features not captured by the

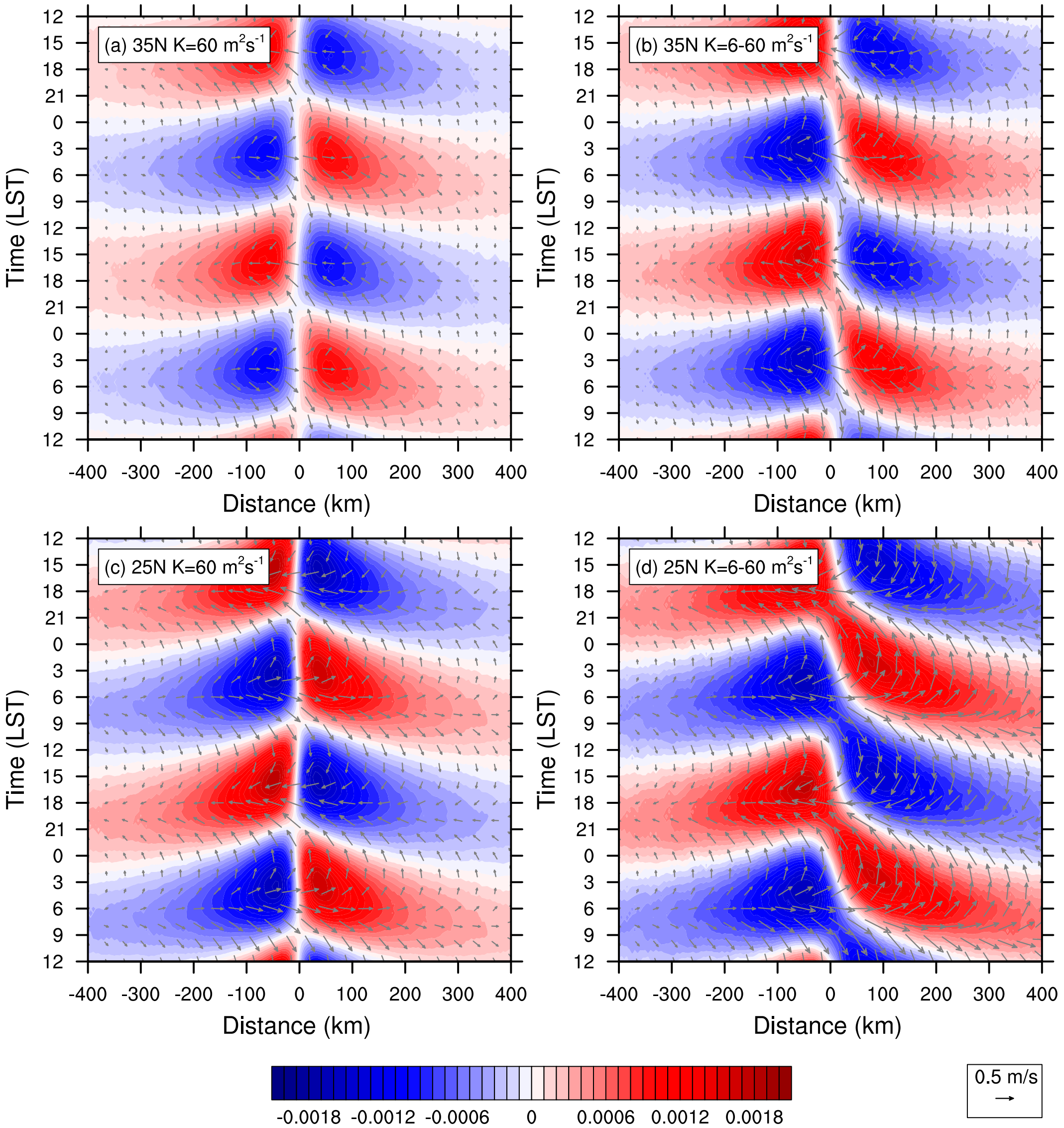

FIG. 10. Longitude distance–time Hovmöller diagrams (over the land on left and sea on right; distance = 0 is coast; the amplitude of diurnal heat flux is 100 W m^{-2} over the land) of perturbation horizontal wind vectors and vertical velocity at 950 hPa (shaded; m s^{-1}) at (a),(b) 35° and (c),(d) 25°N for vertical diffusion coefficient for heat and momentum equal to (a),(c) 60 m^2 s^{-1} everywhere and (b),(d) 60 m^2 s^{-1} over the land and 6 m^2 s^{-1} over the sea from the idealized WRF simulations without terrain.

present linear theory will be discussed in the next section, which describes several simplified mesoscale model simulations.

4. Idealized simulations with terrain heating

a. Configuration of idealized WRF Model

ARW version 3.6 (Skamarock and Klemp 2008) was used to simulate an idealized sea breeze with a 2D domain spanning 3000 km in the *x* direction with horizontal resolution of 5 km and 40 vertical layers. The land occupies 1000 km in the middle of the domain with the sea on either side; periodic boundary conditions are imposed. The initial vertical profile of potential temperature was set to have a constant vertical gradient of 5 K km^{-1}, no moisture, and zero background wind. The heat flux at the land surface was specified as a diurnal variation and zero over the ocean and with zero surface stress everywhere; no radiation or boundary layer parameterizations are used. The horizontal diffusion for momentum and heat was set to zero and the vertical diffusion for heat varied according to the experiment. The vertical diffusion

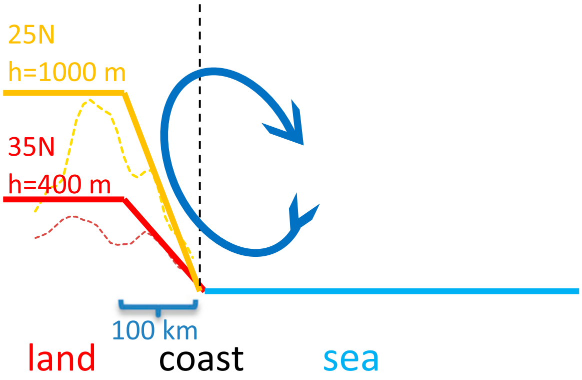

FIG. 11. A schematic diagram showing the circulation near the coast with terrain for two of the terrain profiles used (yellow: 25°N, red: 35°N; solid lines represent the terrain used in the idealized model; dashed lines represent the terrain from the Du model data).

for momentum and the latitude (Coriolis parameter) are control parameters for the sensitivity experiments. The basic numerical simulation starts at 1300 LST (when the heat flux at the surface peaks based on the Du model data) and is integrated forward long enough for the emergence of the diurnally periodic solution which was achieved after 5 days. The results shown in this study are for the fifth day. The detailed configurations and control parameters are shown in Table 1.

b. *Simulations without terrain*

In this section we compare the numerical simulations of the land–sea breeze without terrain from the idealized 2D WRF Model against the Du model data (section 2) and the present linear theory (section 3).

First, in order to check that the model can obtain similar results to the linear theory, we set the amplitude of the diurnal heat flux over land to the relatively small value of 20 W m^{-2}; this together with the relatively small vertical diffusion coefficient for heat of 6 m^2 s^{-1} keeps the vertical gradient of potential temperature stable and the level of diffusion consistent with the linear theory (EXP 1–4 in Table 1).

Figures 9a and 9c show *x–t* Hovmöller diagrams of the offshore vertical motion and wind vectors at 950 hPa with a small vertical diffusion coefficient for momentum (1 m^2 s^{-1}, which corresponds to nearly zero friction in the linear theory) at 35° and 25°N, respectively (EXP 1 and 2 in Table 1). The main features with respect to propagation are consistent with those from the present linear theory (Figs. 7a and 7c): the vertical motion at 25°N exhibits a significant offshore-propagation signal (Fig. 9c), whereas the time phase of vertical motion at 35°N is generally independent of the offshore coordinate (Fig. 9a). An important physical distinction with the present linear theory is that the peak vertical motion in both cases occurs about 3 h later than it does in the linear theory because the vertical transport of heat from the surface takes time in the idealized WRF Model, whereas the atmosphere is heated simultaneously in the whole column in the present linear model.

With larger vertical diffusion for momentum (6 m^2 s^{-1}; EXP 3 in Table 1), the peak at 35°N occurs an additional 2 h later (around 0500 LST) than that in the case with smaller vertical diffusion for momentum (cf. Figs. 9a and 9b) and is now much closer to the absolute time phase from the Du model data (Fig. 2a). At 25°N, with larger vertical diffusion for momentum (EXP 4 in Table 1), the peak occurs 2 h earlier than it does with smaller vertical diffusion for momentum (cf. Figs. 9c and 9d). The time-phase differences due to friction are consistent with results from the linear theory (Figs. 6 and 7).

Simulations with more realistic values and horizontal distributions of heat flux and diffusivity are now described (EXP 5–8 in Table 1). We have performed WRF idealized experiments that use a larger heat-flux amplitude (100 W m^{-2}, which is closer to that found in the Du model data). To avoid convectively unstable profiles of potential temperature with larger heat flux, the vertical diffusion for heat and momentum were increased to 60 m^2 s^{-1} (this value is also reasonable for the diurnally averaged vertical diffusion from the Du model data). We found that the propagation properties for 35°N and 25°N (EXP 5 and 6 in Table 1) are very similar owing to larger vertical diffusion (Figs. 10a and 10c) as we expect from the linear theory (Fig. 3).

However, in reality, the vertical diffusion is very small over the sea. Hence we performed additional WRF idealized experiments, where the vertical diffusion for heat and momentum is set to 60 m^2 s^{-1} over the land and 6 m^2 s^{-1} over the sea (consistent with the Du model data). Figures 10b and 10d show that the propagation properties are different over the land and sea as a result of different vertical diffusion effects on either side of the coastline. The propagation properties for 35° and 25°N (EXP 7 and 8 in Table 1) over the sea in this experiment are similar to those in the cases with small diffusion everywhere and small diurnal heat-flux amplitude (Fig. 9), which in turn are well described by the present linear theory (Fig. 7b and 7d).

c. *Simulations with terrain*

At 25°N, Figs. 9c,d show that the peaks of vertical motion at the coast occur about 4–5 h later than that from Du model data (Fig. 2b), though their propagation properties are similar. At 35°N, an absolute time-phase difference at the coast also exists (Fig. 2a and Fig. 9b). The locations of the maximum amplitude are still away from the coast, similar to the linear theory, but different from the Du model data where the

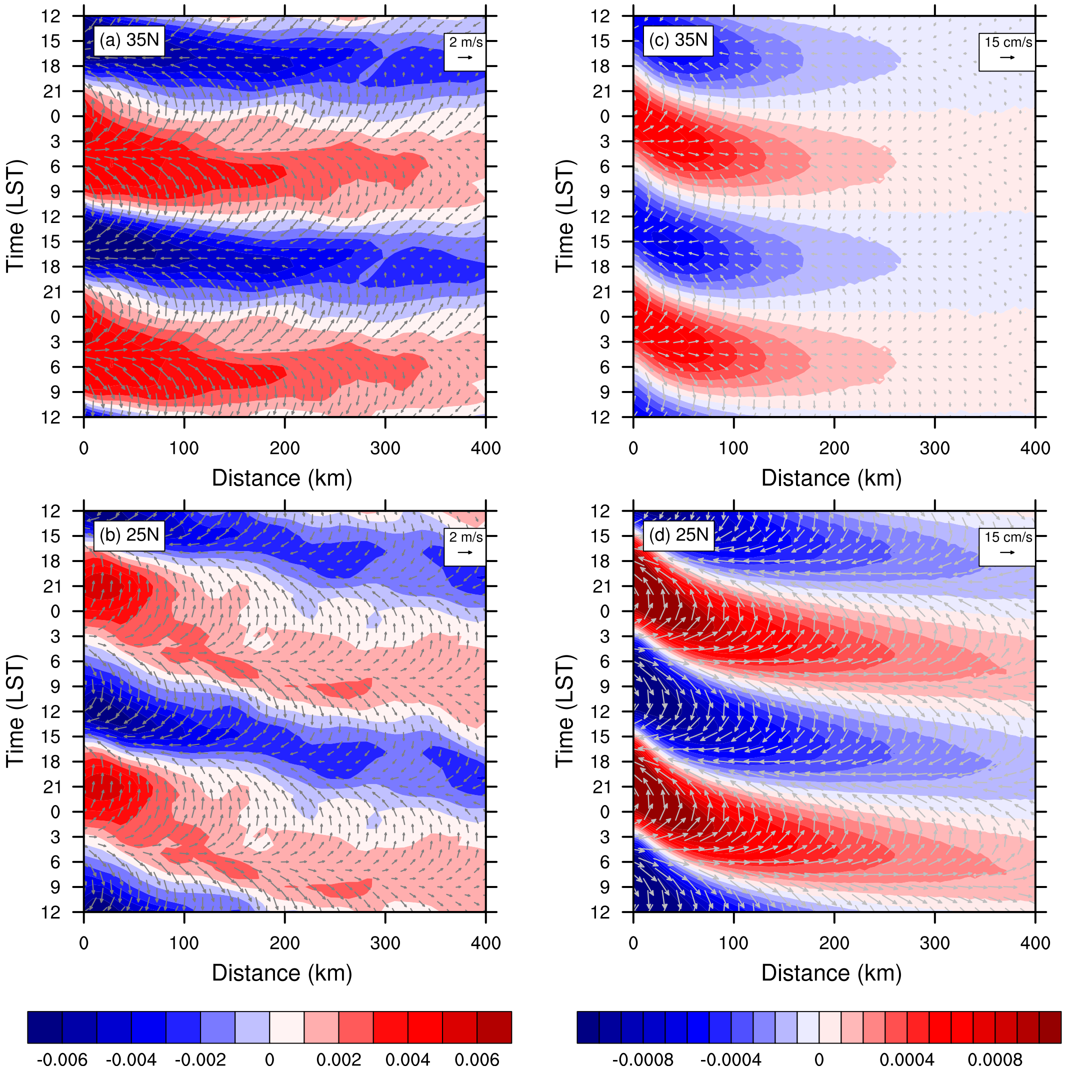

FIG. 12. Longitude distance–time Hovmöller diagrams of perturbation horizontal wind vectors and vertical velocity at 950 hPa (color shaded; m s^{-1}) averaged over the (a) northern and (b) southern boxes in Fig. 1 from the Du model data; idealized WRF experiments with terrain and surface heating at latitudes (c) 35° and (d) 25°N. In the idealized WRF experiments, the amplitude of diurnal heat fluxes is 20 W m^{-2} and the vertical diffusion coefficients for heat and momentum are both 6 $m^2 s^{-1}$.

maxima occur at the coast. We hypothesize that this difference comes from the effect of coastal terrain (Fig. 1). The idealized WRF Model allows us to add coastal terrain and examine its effect.

Based on the terrain height and magnitude of the slope in Du model data, a simple smooth terrain was added near the coast over the land in the idealized model (see Fig. 11). Figures 12c,d show, with coastal terrain, the *x*–*t* Hovmöller diagrams of the offshore vertical motion and wind vectors at 950 hPa with the small amplitude of diurnal heat flux (20 W m^{-2}) and vertical diffusion coefficient for heat and momentum (6 $m^2 s^{-1}$) at 35° and 25°N (EXP 3 and 4 with terrain). The peaks at and near the coast occur earlier than those without terrain (Figs. 9b and 9d) because the coastal mountain acts as an elevated heat source and produces a thermal difference sooner aloft than in the no-mountain case where the diffusion takes several hours to heat the air at higher altitudes. Hence the mountain heating produces a peak at the coast that is earlier than in the case without the mountain. The coexistence of a mountain–valley circulation and a land–sea circulation leads to the maximum amplitudes of vertical motion at the coast (see diagram in Fig. 11). The idealized simulations with terrain (Figs. 12c,d) are much more similar (compared with the present

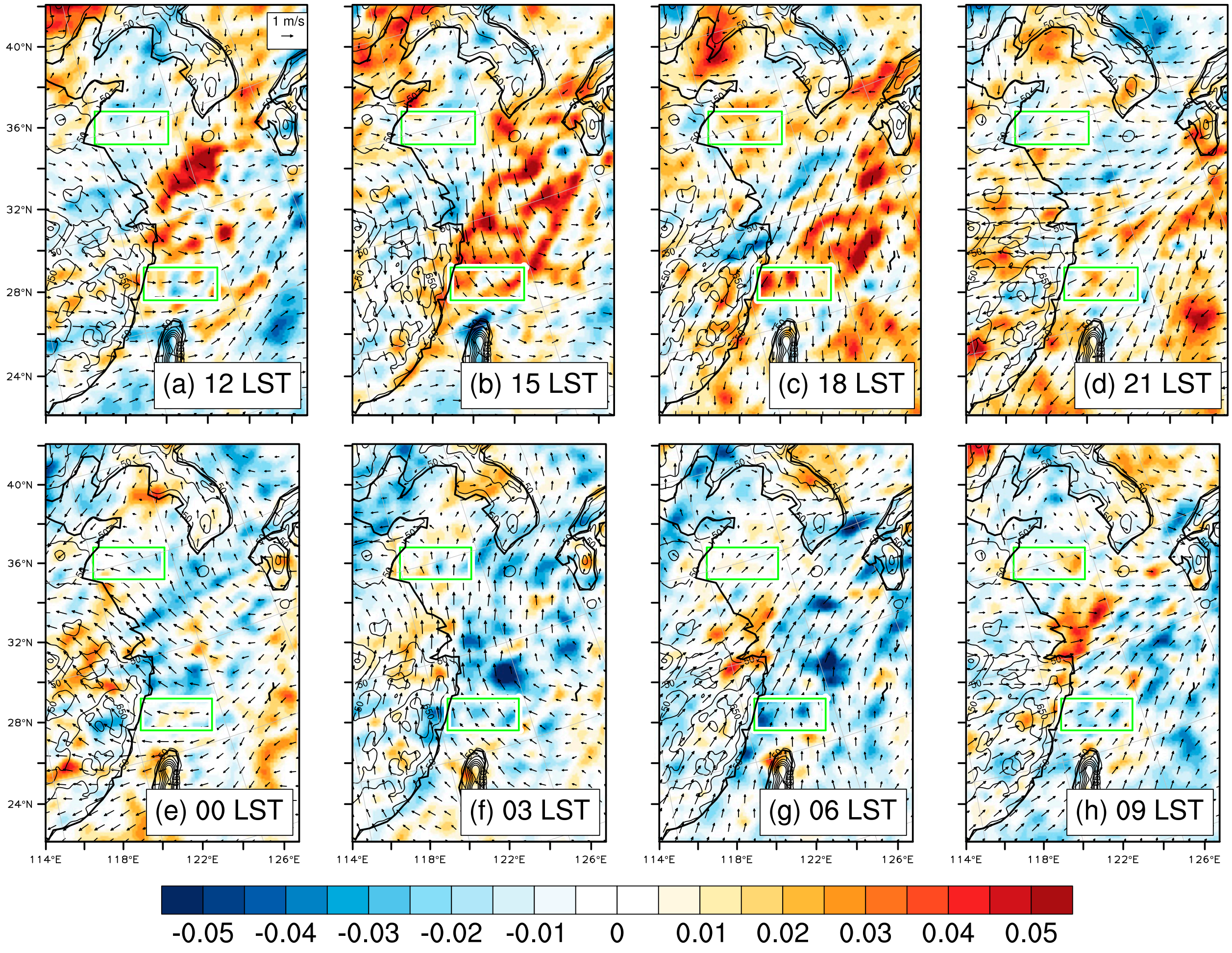

FIG. 13. Diurnal variation of perturbation horizontal wind vectors [reference vector at top right of (a) =1 m s^{-1}] and potential vorticity (color shaded; PVU) at 700 hPa at (a) 1200, (b) 1500, (c) 1800, (d) 2100, (e) 0000, (f) 0300, (g) 0600, and (h) 0900 LST averaged over June 2006–11; selected contours show the terrain height (m).

linear theory) to the results from the Du model data (Figs. 12a,b) with respect to absolute time phase, location of maximum amplitude, and propagation characteristics.

5. Summary and concluding remarks

Long-term (June 2006–11) hourly high-resolution model data (9-km horizontal resolution and 40 vertical levels) simulated with a mesoscale model (WRF) from 12- to 36-h simulations of each day (Du et al. 2014) were used to explore the thermally driven diurnally periodic wind signals off the east coast of China. A linear land–sea-breeze model with friction and an idealized version of the WRF Model with terrain are applied to explain the wind-signal characteristics.

The Du model data indicate offshore eastward propagation of the vertical motion in the boundary layer off the southeast coast of China while the diurnal signal in vertical motion is closer to phased locked off the northeast coast of China. Off the coast of northeastern China, the perturbation horizontal winds are almost westerly (easterly) in the early morning (afternoon) without longitudinal variation for direction, whereas over southeastern China the time phase of the perturbation wind vectors varies with offshore distance. The maximum amplitudes of the diurnal cycles of vertical motion are both at the coast for the northeast and southeast coasts of China.

The present linear land–sea-breeze model indicates that circulations for high latitude and low latitude exhibit different time phases and offshore propagation signals, similar to what is found in the Du model data. With increasing friction, the absolute time phase and the degree of propagation change and are more in agreement with the Du model data. However, differences between the present linear land–sea-breeze model and the Du model data still exist regarding the absolute time phase and the location of the maximum amplitude of the diurnally varying winds.

Because of heat transport from the surface, the idealized land–sea-breeze model using a simplified version of WRF has a phase lag with respect to the linear model that brings the absolute time phase closer to that from the Du model data. With coastal terrain in the idealized model, the maximum amplitude becomes located at the coast and the maximum occurs earlier at and near the coast as compared to the situation without terrain and provides the closest match to the Du model data.

In this paper, we neglected the mean wind in the linear theory, because we focus on the low levels where the background wind (not shown) is small. Li and Smith (2010) suggested that with periodic heating, a westerly mean wind at upper levels can advect diurnal pulses of potential vorticity (PV) generated by imposed heating over the Rockies. To investigate this possibility in the context of the region studied here, we have computed the PV and wind perturbations at 3-h intervals at 700 hPa (Fig. 13), which corresponds to the lower altitude of the coastal mountains as compared to the Rockies. Inspection of Fig. 13 does not show a PV anomaly originating over the mountains late in the day (Figs. 13 c–e) but rather a large-scale PV oscillation over the ocean that moves eastward. The influence of this feature on the flow in the analysis boxes in the coastal zone appears to be slight to negligible since the large-scale feature forms far offshore and then moves eastward. Close inspection of the flow in the analysis boxes of Figs. 1 and 13 strongly suggests to us a sea-breeze circulation influenced by the earth's rotation. Further investigation of this large-scale PV feature would be interesting but is beyond the scope of this paper.

This paper only focuses on the thermally driven diurnal wind signals off the east coast of China rather than patterns of diurnal precipitation. The relationship between winds and precipitation is an important problem that we hope to study in the future.

Acknowledgments. This study is supported by the Chinese 973 program 2013CB430104 and the Chinese National Science Foundation under Grants 40921160380, 4141101075, 41461164006, and 41330421. The first author gratefully acknowledges financial support from the China Scholarship Council. The authors are thankful to Chris Davis and Joe Klemp for internal reviews, three anonymous reviewers for their valuable comments, and Fuqing Zhang and Qinghong Zhang for fruitful discussions.

REFERENCES

Bao, X., F. Zhang, and J. Sun, 2011: Diurnal variations of warm-season precipitation east of the Tibetan Plateau over China. *Mon. Wea. Rev.,* **139,** 2790–2810, doi:10.1175/MWR-D-11-00006.1.

Carbone, R. E., J. D. Tuttle, D. A. Ahijevych, and S. B. Trier, 2002: Inferences of predictability associated with warm season precipitation episodes. *J. Atmos. Sci.,* **59,** 2033–2056, doi:10.1175/1520-0469(2002)059<2033:IOPAWW>2.0.CO;2.

Drobinski, P., R. Rotunno, and T. Dubos, 2011: Linear theory of the sea breeze in a thermal wind. *Quart. J. Roy. Meteor. Soc.,* **137,** 1602–1609, doi:10.1002/qj.847.

Du, Y., and R. Rotunno, 2014: A simple analytical model of the nocturnal low-level jet over the Great Plains of the United States. *J. Atmos. Sci.,* **71,** 3674–3683, doi:10.1175/JAS-D-14-0060.1.

——, Q. H. Zhang, Y. L. Chen, Y. Y. Zhao, and X. Wang, 2014: Numerical simulations of spatial distributions and diurnal variations of low-level jets in China during early summer. *J. Climate,* **27,** 5747–5767, doi:10.1175/JCLI-D-13-00571.1.

——, Y. Chen, and Q. Zhang, 2015a: Numerical simulations of the boundary layer jet off the southeastern coast of China. *Mon. Wea. Rev.,* **143,** 1212–1231, doi:10.1175/MWR-D-14-00348.1.

——, R. Rotunno, and Q. Zhang, 2015b: Analysis of WRF-simulated diurnal boundary-layer winds in eastern China using a simple 1D model. *J. Atmos. Sci.,* **72,** 714–727, doi:10.1175/JAS-D-14-0186.1.

Garreaud, R. D., and R. Muñoz, 2004: The diurnal cycle in circulation and cloudiness over the subtropical southeast Pacific: A modeling study. *J. Climate,* **17,** 1699–1710, doi:10.1175/1520-0442(2004)017<1699:TDCICA>2.0.CO;2.

Gille, S. T., S. G. Llewellyn Smith, and N. M. Statom, 2005: Global observations of the land breeze. *Geophys. Res. Lett.,* **32,** L05605, doi:10.1029/2004GL022139.

Haurwitz, B., 1947: Comments on the sea-breeze circulation. *J. Meteor.,* **4,** 1–8, doi:10.1175/1520-0469(1947)004<0001:COTSBC>2.0.CO;2.

He, H., and F. Zhang, 2010: Diurnal variations of warm-season precipitation over northern China. *Mon. Wea. Rev.,* **138,** 1017–1025, doi:10.1175/2010MWR3356.1.

Jiang, Q., 2012a: On offshore propagating diurnal waves. *J. Atmos. Sci.,* **69,** 1562–1581, doi:10.1175/JAS-D-11-0220.1.

——, 2012b: A linear theory of three-dimensional land–sea breezes. *J. Atmos. Sci.,* **69,** 1890–1909, doi:10.1175/JAS-D-11-0137.1.

Li, Y., and R. B. Smith, 2010: The detection and significance of diurnal pressure and potential vorticity anomalies east of the Rockies. *J. Atmos. Sci.,* **67,** 2734–2751, doi:10.1175/2010JAS3423.1.

Mapes, B. E., T. T. Warner, and M. Xu, 2003: Diurnal patterns of rainfall in northwestern South America. Part III: Diurnal gravity waves and nocturnal offshore convection. *Mon. Wea. Rev.,* **131,** 830–844, doi:10.1175/1520-0493(2003)131<0830:DPORIN>2.0.CO;2.

Muñoz, R. C., 2008: Diurnal cycle of surface winds over the subtropical southeast Pacific. *J. Geophys. Res.,* **113,** D13107, doi:10.1029/2008JD009957.

Qian, T., C. C. Epifanio, and F. Zhang, 2009: Linear theory calculations for sea breeze in a background wind: The equatorial case. *J. Atmos. Sci.,* **66,** 1749–1763, doi:10.1175/2008JAS2851.1.

Rahn, D. A., and R. Garreaud, 2010: Marine boundary layer over the subtropical southeast Pacific during VOCALS-Rex. Part 1: Mean structure and diurnal cycle. *Atmos. Chem. Phys.,* **10,** 4491–4506, doi:10.5194/acp-10-4491-2010.

Rotunno, R., 1983: On the linear theory of the land and sea breeze. *J. Atmos. Sci.,* **40,** 1999–2009, doi:10.1175/1520-0469(1983)040<1999:OTLTOT>2.0.CO;2.

Schmidt, F. H., 1947: An elementary theory of the land- and sea-breeze circulation. *J. Meteor.,* **4,** 9–20, doi:10.1175/1520-0469(1947)004<0009:AETOTL>2.0.CO;2.

Skamarock, W. C., and J. B. Klemp, 2008: A time-split nonhydrostatic atmospheric model for weather research and forecasting applications. *J. Comput. Phys.,* **227,** 3465–3485, doi:10.1016/j.jcp.2007.01.037.

Sun, J., and F. Zhang, 2012: Impacts of mountain–plains solenoid on diurnal variations of rainfalls along the mei-yu front over the east China plains. *Mon. Wea. Rev.,* **140,** 379–397, doi:10.1175/MWR-D-11-00041.1.

Trier, S. B., C. A. Davis, D. A. Ahijevych, M. L. Weisman, and G. H. Bryan, 2006: Mechanisms supporting long-lived episodes of propagating nocturnal convection within a 7-day WRF Model simulation. *J. Atmos. Sci.,* **63,** 2437–2461, doi:10.1175/JAS3768.1.

Wang, C. C., G. T. J. Chen, and R. E. Carbone, 2004: A climatology of warm-season cloud patterns over East Asia on GMS infrared brightness temperatures observations. *Mon. Wea. Rev.,* **132,** 1606–1629, doi:10.1175/1520-0493(2004)132<1606:ACOWCP>2.0.CO;2.

——, ——, and ——, 2005: Variability of warm-season cloud episodes over East Asia based on GMS infrared brightness temperature observations. *Mon. Wea. Rev.,* **133,** 1478–1500, doi:10.1175/MWR2928.1.

Wood, R., M. Köhler, R. Bennartz, and C. O'Dell, 2009: The diurnal cycle of surface divergence over the global oceans. *Quart. J. Roy. Meteor. Soc.,* **135,** 1484–1493, doi:10.1002/qj.451.

Xu, W., and E. J. Zipser, 2011: Diurnal variations of precipitation, deep convection, and lightning over and east of the eastern Tibetan Plateau. *J. Climate,* **24,** 448–465, doi:10.1175/2010JCLI3719.1.

Yang, G., and J. Slingo, 2001: The diurnal cycle in the tropics. *Mon. Wea. Rev.,* **129,** 784–801, doi:10.1175/1520-0493(2001)129<0784:TDCITT>2.0.CO;2.

Yu, R., T. Zhou, A. Xiong, Y. Zhu, and J. Li, 2007: Diurnal variations of summer precipitation over contiguous China. *Geophys. Res. Lett.,* **34,** L01704, doi:10.1029/2006GL028129.